

1N-93-CR  
65151

P-48

The magnetic evolution of AR 6555 which lead to  
two impulsive, relatively compact, X-type flares.

J.M. Fontenla<sup>1</sup>

*The University of Alabama in Huntsville,  
EB-136M CSPAR, Huntsville, AL 35899*

A. Ambastha<sup>2</sup>

*NRC/National Academy of Sciences,  
ES-52 Space Science Laboratory,  
NASA/Marshall Space Flight Center,  
Huntsville, AL 35812*

N96-16588

Unclass

63/93 0065151

B. Kalman, and Gy. Csepura

*Heliophysical Observatory of the Hungarian Academy of Sciences,  
H-4010 Debrecen, P.O.B. 30,  
Hungary*

(NASA-CR-199317) THE MAGNETIC  
EVOLUTION OF AR 6555 WHICH LEAD TO  
TWO IMPULSIVE, READILY COMPACT,  
X-TYPE FLARES (NASA. Marshall  
Space Flight Center) 48 p

Received: 1993 December 8

Revised: 1994 July 15

<sup>1</sup> Present address, High Altitude Observatory, P.O. Box 3000, Boulder, CO 80307.

<sup>2</sup> Present address, Udaipur Solar Observatory, 11 Vidya Marg, Udaipur 313001, India.

### Abstract

We study the evolution of the vector magnetic field and the sunspot motions observed in AR 6555 during 1991 March 23-26. This region displays two locations of large magnetic shear that were also sites of flare activity. The first location produced two large (X-class) flares during the period covered by our observations. The second location had larger magnetic shear than the first, but produced only small (M- and C-class) flares during our observations. We study the evolution of the photospheric magnetic field in relation to the large flares in the first location. These flares occurred around the same included polarity, and have very similar characteristics (soft X-ray light curves, energies, etc.). However, the whole active region has changed substantially in the period between them. We found several characteristics of the region that appear related to the occurrence of these flares. 1) The flares occurred near regions of large magnetic "shear", but not at the locations of maximum shear or maximum field. 2) Potential field extrapolations of the observed field suggest that the topology changed, prior to the first of the two flares, in such a way that a null appeared in the coarse magnetic field. 3) This null was located close to both X-class flares, and remained in that location for a few days while the two flares were observed. 4) The flaring region has a pattern of vector field and sunspot motions in which material is "squeezed" along the polarity inversion line. This pattern is very different from that usually associated with shearing arcades, but it is similar to that suggested previously by Fontenla and Davis (1991). The vertical electric currents, inferred from the transverse field, are consistent with this pattern. 5) A major reconfiguration of the longitudinal field and the vertical electric currents occurred just prior to the first of the two flares. Both changes imply substantial variations of the magnetic structure of the region. On the basis of the available data we suggest that these changes made the flaring possible, and we develop a scenario that can explain the origin of the magnetic free-energy that was released in these flares.

*Subject Heading:* Sun: flares-Sun: magnetic fields-Sun: X-rays, gamma rays.

## 1. Introduction

An outstanding problem in the physics of the outer layers of the Sun is the physical mechanism that builds up magnetic free-energy and releases it in solar flares. The production of major flares is expected to be closely related to some particular properties of photospheric magnetic fields. Suggested properties include: particular values of magnetic field, gradients, shear, sunspot motions, and magnetic field patterns that may indicate the probability and magnitude of an impending flare. The identification of the relevant properties is important for developing and testing theoretical models, and for forecasting flare activity.

However, observations point in different directions regarding the properties of flaring active regions. For instance, it has been long known that, statistically, the most flare-active regions are the "delta" configurations where opposite polarity sunspots are intermingled in a common penumbra (e.g. Kunzel 1960). Also, it is known that the most dynamic regions are more flare prone (e.g., see Tandberg-Hanssen and Emslie 1988); and more recently it has been shown that many flares occur in highly "sheared" active regions (Hagyard et al. 1984).

All the above mentioned properties derive from statistics over many active regions, and sometimes a particular flaring active region may not show these properties. Moreover, some active regions having these properties produce no large flares. Known indicators of a flare-prone situation may not, therefore, fully determine the occurrence of a flare. Other active-region properties that are sometimes related to flares are emerging and canceling flux (e.g. Heyvaerts, Priest and Rust 1977, Livi et al 1989). Their roles are still controversial and a number of examples and counter-examples are found in the literature.

Each of the previously mentioned characteristics of the flaring active regions has influenced theories of flare buildup (e.g., see reviews by Svestka 1976, and Sturrock 1980): emerging flux is central to the model by Heyvaerts, Priest and Rust (1977), in

which a current sheet forms as a result of the action of new flux against pre-existing flux; magnetic shear spawned a variety of flare scenarios based on a sheared arcade (e.g., Sakurai 1989) or a twisted loop (e.g., Spicer 1981). Other studies suggested that flares arise from the interaction between loops in adjacent active regions (e.g., Machado 1987). Recently, two particular features have been related to the occurrence of major flares: according to Leka et al. (1993), and de la Beaujardiere, Canfield and Leka (1993) the locations of vertical currents derived from photospheric vector magnetograms are close to flare kernels; and Demoulin, Henoux, and Mandrini (1992) suggest that magnetic "separatrices" are the locations where flares originate.

Many of the above-mentioned characteristics and models appear, at first sight, as unrelated, and some are mutually exclusive from a theoretical standpoint. There is no compelling evidence that all flares, of all magnitudes and various spatial, and temporal behavior, must share the same configuration of the magnetic field and identical process to build-up magnetic free-energy. Moreover, some disparate cases have been observed in which it seems that no single model may apply to all stages of the observed flares. Therefore, we must keep an open mind, and accept that similar basic plasma processes for energy storage and release may occur that lead to various kinds of flares in several different magnetic configurations (Gaizauskas 1989). We need to examine many cases in detail for establishing the ways an active region may develop to a flare-prone situation, and to extract the relevant properties of the magnetic field.

In this paper we will not try to single out a "cause" or a particular scenario for all flares. Rather, our goals in this paper are to analyze: 1) how the interpretation of a set of observations may indicate magnetic free-energy buildup; 2) how the observations may indicate the likelihood of occurrence of a particular type of flare. Also, we compare the magnetic structure of flaring and non-flaring parts of an active region to assess the role of various properties related to flaring. In particular we study the shearing of the field, and the large vertical electric currents, that did not lead to flaring

We study observations of the vector magnetic field of the active region AR 6555 for the period 1991 March 23-26, performed at MSFC. These data are supplemented by white-light and sunspot structure and position from the Debrecen Observatory. Earlier study of this region, during the same time period, by Ambastha, Hagyard, and West (1993) concentrated on the characteristics of the observed "shear" through the overall region. Our present study uses similar data but concentrates on different aspects concerning the field topology, the development of electric currents, and the development of magnetic free-energy that may power the flares in this active region.

In the next sections we will describe the basic structure and parameters of the active region and flaring we study. Then we will describe the observed sunspot motions, and the evolution of the coarse structure of the potential field that is inferred from the *vector magnetograms*. In subsequent sections we study the observed departures of the field from the potential case. From these departures, and the sunspot motions, we infer how, in the flaring region, magnetic free-energy appears to build-up in a very specific way. Finally we discuss our interpretation of the observations and their implications for flare models and for flare forecasting schemes.

## 2. The active region

AR 6555 passed across the visible hemisphere from 1991 March 17 to 31 at a solar latitude around  $25\text{-}28^\circ$  South. Our study is centered around the central meridian transit from E20 to W20, and thus is not seriously affected by projection effects. The white-light appearance of the region is shown in Figure 1, which shows the main sunspots of the region labeled for future reference.

## 2.1. The Flaring

In the days preceding our observations flares of M- and C-class occurred, also an X-9.1 event occurred on March 22 at 22:45 UT. Most of these flares were located in the leading complex around P3 and N6, and some of them were quite extended (see Ambastha, Hagyard and West 1993).

During the period of our observations, in contrast, no large flares (X-class) occurred near P3 and N6, even when large shear, vertical currents and field gradients existed at these locations as we show below. The only large flares reported were two X-class flares located near P1: the first on March 25 at 08:10 UT (X5.3), and the second on March 26 at 20:35 UT (X4.7). In this paper we study the evolution of the magnetic field in relation to the occurrence of these two large flares and the absence of large flares near P3 and N6.

## 2.2. The Observed Magnetic Field

The evolution of the longitudinal field structure of the region during the observed period is depicted by Figure 2a. The largest magnitude of the negative longitudinal field is reported at about 2,100-2,200 G by Mount Wilson (the MSFC data is suitably corrected to match these data, as described by Ambastha, Hagyard and West 1993), and corresponds to the large umbra, N1, of the main trailing sunspot group. The largest positive field, reaches only about 1800 G at one of the small leading spots, P5. These spots are well separated from the main trailing group by an area of intermingled polarities. In Table 1 we list, for reference, the maximum values of the field for each of the spots identified in Figure 1. A large flux imbalance is evident: the accumulated positive (leading polarity) flux can only balance 15-18% of the accumulated negative (trailing polarity) flux. This result cannot be accounted for by any reasonable calibration offset. Consequently, we expect that most of the negative flux closes outside the field of view of our magnetograms. There is a neighboring active region farther to the East, another small

active region to the North, and a few small positive spots to the West, but they are not enough to compensate for the missing return positive flux. Therefore, we conclude that much of the return flux should consist of small magnitude longitudinal magnetic field that is extensively spread over a large area, probably through the enhanced network that extends to the East in the Ca II images.

In Figure 2b we present a saturated view of the longitudinal magnetic field (in which all fields larger than +200 G are displayed white and all fields smaller than -200 G are black), in order to show the weaker fields and the main polarity inversion line (hereafter MPIL). This line is located to the East of the main leading spots, P5 and P4, at the region of relatively low fields (the other main leading spot, P6, is at the edge of the field of view). The figure also shows: the complex positive polarity, P3, that invades the negatively dominated area (formed by N3, N4, N5 and N6); the steep field gradients with surrounding negative field small spots; and the included spots, P1 and P2, that surround the main leading spot group, N1 and N2. As shown in the previous figures, these included spots share the same penumbra of the main negative spots. The most significant included polarity related to the flares observed in this period, IP1, is associated with the spot P1. The included polarity IP1 has moderate field of only about 1,100 G (at the beginning of the period). The large-scale pattern of the field is dominantly negative polarity to the West of the MPIL, and essentially positive to the East. This is the expected pattern in this cycle and hemisphere, but it is somewhat atypical in that the trailing flux of AR 6555 is highly concentrated while the leading flux is very spread out. A cartoon showing how the coarse large-scale configuration may be described is shown in Figure 3.

Figure 2 shows the basic evolution of the structure of the longitudinal field during these days. The strip of positive polarity, IP1, as seen on March 23 and 24, broke in two parts (IP1a and IP1b) between the last observation on March 24 and the first on March 25 (at 13:57 UT). The break was at the southeastern-most point, and this location changed from being part of IP1 (positive polarity) into being part of the main trailing sunspot

(negative polarity). This change cannot be explained by projection effects, because the region is not far from central meridian (and close to disk center), and because of the direction of the transverse field (almost perpendicular to the region displacement on the disk between the two days). The basic structure in this part of the active region remained unchanged through March 25 and 26, but the spot P1 associated with one of these fragments (IP1a) drifted away relative to the main negative spots until it finally detached from the common penumbrae.

The first large flare near this location (on March 25) occurred close to the time of the splitting of IP1; a precise timing is not possible because these events occurred during the nighttime at the MSFC (the first observation on March 25 is about 5:47 hours after the flare). The longitudinal field undergoes slow fading after this rupture; however, the transverse field changed more significantly. This change is such that the magnetic shear at IP1a decreased (as did the electric current, see below). However, the second large flare occurred on March 26 at basically the same location and with very similar energy and temporal behavior. This flare, and the vector magnetic fields were observed at MSFC with good temporal resolution (see Ambastha, Hagyard and West 1993).

### 3. Sunspot motions

We derived the proper motions of umbrae in AR 6555 during 1991 March 21-26 from 203 photographic observations, taken at the Debrecen Heliophysical Observatory and its Gyula Observing Station. Details of the method for reducing the measurements are given by Kalman (1980), and Bumba et al. (1993). The heliographic coordinates of the various umbrae, computed in the Carrington System, show a strong backward drift caused by differential motion at the latitude of the sunspot group. Proper motions of the entire group are difficult to assess because of uncertainties in the differential rotation and in differences between the rotation rates of different solar features. For this reason we



consider here only the motions relative to the largest field and most stable umbra N1. Since the individual measurements have a scatter of about 0.15 heliographic degrees, mainly due to atmospheric seeing effects, and there were more than 200 measurements of each long-lived umbra in the course of 6 days, some averaging and smoothing was performed to show the sunspot trajectories. We fitted cubic splines to the mean positions of the umbrae at 12:00 UT on each observing day.

Figure 4a gives the trajectories of the individual umbrae in AR 6555 that was clearly observed for at least two days. In this paper we designate the umbrae in a way resembling the one used in Ambastha, Hagyard and West (1993), namely the leading polarities (positive) are indicated by a prefix P and the following (negative) by a prefix N. Arrowheads represent the position of a given umbra, and its direction of motion, at 12:00 UT every day. The contours in Figure 4b correspond to the umbrae and penumbrae, with heliographic coordinates corrected for differential rotation. These contours show the morphological changes in the active region during 1991 March 21-26.

AR 6555 was dominated by the large complex N1-N2 of irregularly shaped, old following polarity umbrae, dissected by several light bridges. This complex moved eastward slowly with respect to the local standard rotation as is characteristic of old spots. (This eastward motion is not shown in the figure, where all motions are referred to those of the N1-N2 complex.) The most significant changes occurred in the eastern part of the group, where a new pair of polarities (P1-N2) appeared on March 21 in an almost N-S alignment. This new dipole moves to the West as is usual for new spots, and its northernmost part, N2, moves toward the similar polarity old umbra N1. The southernmost part of the new dipole, the included polarity P1, emerged within the southeast penumbra of the old spot N1. This spot grew with a rapid westward motion in the first days, and later moved southward, until it finally detached completely from N1 (on March 26). The other included spot, P2 located to the North-West of N2, also displayed westward motion but of smaller magnitude.

On the western side of N1 spot, N5 and P3 moved significantly: umbra N5 with rapid westward direction; P3 with slower motions. The relative motions of these spots tended to bring them together. During March 23-24, the penumbra of N5 joined that of P3; N5 slowed down and turned southward until both spots moved practically parallel to each other.

The general picture of observed sunspot motions resembles the pattern of a hydrodynamic flow around an obstacle. The role of an obstacle is played by the old, disintegrating large umbra N1. The emerging material that carries the new magnetic flux, shown by N2 and P1, flows around the "obstacle" in its westward motion. Other smaller negative polarity umbrae to the Southeast of N1 also take part in this westward flow. As Figure 4a shows, the trajectory of the spot N7 crosses that of P1, but N7 moves to the West of P1 and the two spots never approach each other.

The full detail of the sunspot motions is given here because it is a critical test for understanding the magnetic field evolution and the scenario that we address in the discussion.

#### 4. The inferred coarse potential field

We computed the coarse potential field that corresponds to the observed vector fields by averaging the measurements over 4x4 pixels (i.e., about 11x11 arc sec). Averages made over 2x2 pixels show no significant differences for our present discussion. Since our fields of view differ for all the dates considered, we extract a sub-field-of-view that was always observed and contains all the relevant features. For this sub-field we carried the averaging of the measured values of all components of the vector field and assigned the resulting value to the center of the 4x4 pixels. This procedure is somewhat crude, but it is adequate for our purpose of finding the *coarse* structure of the potential field.

Details of our procedure for calculating the potential field are described in Appendix A. We describe the potential field by assigning a number of source dipoles to a plane at eight pixels depth beneath the photosphere (twice the separation between the used measurements of the field). The number of dipoles equals the number of points to be matched. In contrast to other methods that consider only vertical dipoles (e.g., Demoulin, Henoux and Mandrini 1992), we consider dipoles with three arbitrary components of the magnetic moment (i.e., dipoles with arbitrary strength and tilt). We find the strength of all three components of the dipoles in such a way that their field matches the observed longitudinal field exactly and matches the transverse field approximately. (The approximation of the transverse field is in the least square sense.) The horizontal components of the field contain important information on how the field lines close. They supplement the lack of constraints on the normal components of the field at the sides and the top of the domain where we compute the potential field. (Keep in mind that the potential field is uniquely defined only when the normal components of the field are given for a *closed* domain where no currents exist.) If the observed horizontal components are not used, and one resorts to purely vertical dipoles, the result for our region in which a large flux imbalance occurs would be unrealistic. The global structure would depart too much from the leading positive and trailing negative polarities that are apparent in large field-of-view magnetograms. Our computed distribution of dipoles contains only a weak vertical component and a much larger horizontal component of the dipole moment.

The resulting potential field lines are complicated because of the mixing of polarities and the complicated distribution of the photospheric field. Since a limited field of view is used, and large non-potential behavior is observed at some locations, the potential field calculated here represents only the one that is closest to the observations. The real coronal magnetic field is expected to differ from the calculated one because of edge effects, and because of electric currents that are known to flow across the photosphere and close within the upper layers.

However, we found an interesting property of the potential field (Table 2). Initially the coarse structure of the potential field evolves only in magnitude but not in topology. No null points of the potential field occur above the photosphere, in the neighborhood of IP1, for the data corresponding to March 23. But, on March 24 (several hours before the flare) a local minimum of the magnitude of the field or quasi-null,  $B \sim 7$  G, appears above the location in the photosphere where the polarity IP1 later broke up. Then, on the 25th ( $\sim 6$  hours after the first flare) the local minimum evolved into a full null of the field, having zero absolute value, and shifted to the West. For the potential field of the 26th, the null remained more or less at the same location but shifted slightly further to the West. These data show that a large qualitative change in the coarse potential field topology took place between March 24 and 25, in coincidence with the onset of the flare activity at the location of IP1a.

The qualitative change is also apparent in some of the field lines (not shown) that can be computed from the potential field. The changes of the potential-field structure after March 25 are not very significant. Instead, the changes between March 24-25 are substantial, and correspond to a split of the eastern fieldlines from the eastward directions they have on March 24 into northward and southward lines. These changes, and the appearance of the potential field null are consequences of the changes that the photospheric field was undergoing, particularly when IP1 split into IP1a and IP1b. The change in the structure of the potential field seems spatially and temporally related to the beginning of major flare activity at IP1a, although the theoretical reasons are not clear (but see the discussion *f7*). Furthermore, the fundamental changes that the active-region structure was undergoing are hinted already by the appearance of a quasi-null late on March 24 (many hours before flaring starts). These changes were not apparent in the raw magnetograms on March 24, but were clear in the data corresponding to the following day.

## 5. Departures from the potential field

The departures of the observed field from a potential one can be characterized in two ways: by the angles between the observed and potential transverse field, or by the inferred vertical electric currents. The angle is relatively unaffected by calibration of the measurements in the regions of weak longitudinal field. The vertical currents are, however, strongly affected by calibration of the transverse field. Both, the angle and the currents are dependent on the arbitrary criteria used for resolving the  $180^\circ$  ambiguity of the transverse field azimuth.

In addition, any comparisons rely heavily on the somewhat arbitrarily selected potential field (see Appendix A). Our analysis uses the potential field that was calculated as described in the previous section. However, we also compared our results for the departures with those corresponding to the potential field obtained following a previous scheme (Teuber, Tandberg-Hanssen, E., and Hagyard 1977). We found that the qualitative behavior of the shear angle does not differ much (except at a few locations). More significant differences occur in the magnitude of the transverse field; our method gives generally smaller values of the transverse field that are closer to the observed. Since non-potential behavior is clear in either case, it is hard to make a strong case for the appropriateness of any scheme for computing the potential field. The potential field derived in this paper gives the photospheric *vector* field that is closest to the observed field. Therefore, the departures of the observed from the potential field are *minimized* in our scheme.

The angle between observed field and the calculated potential field, near the inversion lines of the longitudinal component, has been characterized as the "shear" of the observed magnetic field. This idea was extended to locations removed from the inversion line by Ambastha, Hagyard and West (1993) for this particular active region.

In Figure 5 we show contours of the vertical electric current inferred from the MSFC vector field measurements for the four consecutive days. The vertical electric current density,  $J_z$ , is determined as indicated in Appendix B. Comparing the vertical currents with the "magnetic shear" shown by Ambastha, Hagyard and West (1993) in their Figure 3 it is clear that contours of maximum currents occur at some of the edges of contours of maximum shear.

The temporal changes observed in the current's pattern are shown in Figure 5. These changes are much more drastic than those displayed by the shear, but the directions of their changes coincide. This indicates that although currents are localized, they affect large areas. On March 23 there are several kernels of large currents near the polarity inversion line between IP1 and N1, hereafter current system A. The most extended kernels correspond to positive values (upflowing currents); only part of the negative return currents is visible. There is another current system at the line that half encloses the positive polarity around P3, hereafter current system B, and there is a third one on both sides of the polarity inversion line between P2 and N2, hereafter current system C. Systems B and C are much more balanced than A, and they display more or less as much upflowing as downflowing currents. The quantitative behavior of the currents is shown in Table 3 for the three main current systems.

On March 24 system A fractured in several parts, decreased from the values discussed above, and almost half-encircled the spot N1. System B gained strength and became more compact as its sunspots approached each other. System C decreased somewhat in intensity and became more fragmented. At this time, the strongest current system in the entire active-region is B, while system A is far less intense.

On March 25, after the first of the two X-class flares, system A changed drastically. This change coincides with the restructuring of the longitudinal field and with the motions of the spot P1 across the penumbra of N1. Since all these changes were

observed simultaneously one cannot draw any conclusion regarding a cause and effect relationship. The changes were most likely the result of photospheric motions and deeper seated forces acting on the photospheric plasma and magnetic field. The structural change of system A replaces the previous pattern with: a pair of oppositely directed semicircles of strong currents that are more or less in balance and another pair of oppositely directed currents displaced to the West (and very close to IP1a). The changes in the other current systems are much less impressive. The northern components of system B diminished and the southern components intensified; system C practically dissolved, showing only a pair of small kernels. At this time system A was as strong as system B.

On March 26, before the second X-class flare, current system A had simplified into two strip currents: one upflowing in the North, the other downflowing in the South. These strips were located between N1 and the now fully detached P1. The intensity of this current system had severely decreased, consistently with the decrease in the "shear index" at this location. Current system B continued the same trend of evolution; its northernmost portions decreased and fragmented, while the southernmost portion enhanced and organized. At this time the remnants of system C were barely visible above the noise.

Comparing the sunspot motions and the vertical currents, it is evident that they coincide, and are well related to the observed transverse field pattern (e.g., see Figure 5 in Ambastha et al 1993). All these quantities indicate that the field in the region between IP1, and later IP1a, and N1 was stressed by horizontal flows in the South-West and West directions. The flows have maximum velocity near the polarity inversion line, and also produced some rotation of magnetic features. The motion pattern was quite different from that usually assumed in numerical simulations of shearing arcades. In Figure 6 we compare (looking down toward the photosphere) the usual flow and sheared field pattern with that proposed by Fontenla and Davis (1991). The conventional shear pattern has zero velocity at the polarity inversion line, a maximum absolute value on each side of this line, and a change of sign across the polarity inversion line. This pattern produces field distortions

and electric currents that are very different from those observed near IP1 and IP1a. The pattern of vertical currents corresponding to the usual shear flow also changes sign at the longitudinal field polarity-inversion-line, and also reaches a maximum absolute value on either side.

The flow, transverse field, and vertical current patterns that Fontenla and Davis (1991) propose are quite different: a maximum of the current density at the inversion line, at the location of maximum velocity, and much weaker and spread out return currents at both sides. This pattern is much closer to the observed, although the maximum current and horizontal velocity are not exactly at the longitudinal field inversion line, but are offset toward IP1 (later IP1a). The return currents are not observed, probably because they are masked by noise due to their more spread out distribution.

## 6. Magnetic free-energy buildup

The buildup of free-magnetic energy in the upper atmospheric layers can be studied by computing the work done by the Lorentz force at the photospheric layers. This quantity corresponds to the Poynting vector at the photosphere (see Krall and Trivelpiece 1973), and gives an upper limit to the rate of magnetic free-energy buildup. The part that is available for flaring is stored above the photosphere in the form of field-aligned currents, without being dissipated or dispersed.

The power upflow can be computed from the magnetic field and the electric current that give rise to the Lorentz force, and the plasma velocity. From our observations we can only deduce horizontal velocities,  $V_h$ , and vertical electric currents,  $J_z$ . Vertical velocities and horizontal currents are undetermined by our observations. Consequently the full power supplied cannot be found. From our data, however, we can obtain one of the components of this power.



The vertical component of the current, together with the horizontal component of the field, give part of the horizontal component of the Lorentz force,  $F_h = J_z \times B_t$ . Another contribution to the horizontal force may come from horizontal currents and vertical fields (except at the polarity inversion line where the vertical component of the field vanishes). Thus, the horizontal Lorentz force plotted in Figure 7 may not represent the total horizontal Lorentz force at locations remote from the polarity inversion line (if horizontal currents are present). Figure 7 shows that the most significant horizontal forces occur very close to the polarity inversion lines; thus they practically correspond to the total horizontal Lorentz forces. Note their different alignment with respect to the polarity inversion line in current systems A and B. On March 23 and 24 the forces at system C are smaller and have a similar pattern to those at B; then they practically vanish on March 25 as the remainder shifts away from the inversion line on March 26. The differences between the forces at systems A and B are closely related to the previously discussed differences in the current patterns.

The forces at system B, on the northern side on March 23 and 24, and on the southern side on March 26, point *away* from the polarity-inversion-line. Their largest magnitude is about  $10^{-3} \text{ N m}^{-2}$ ; there are opposing forces of comparable magnitude at each side of the inversion line. Since the observed horizontal motions press the material toward the inversion line, we find that work is done by mechanical over electromagnetic forces, and therefore there is feeding of mechanical into electromagnetic energy. This corresponds to the observed buildup of vertical currents of opposite sign at each side of the inversion line, much like the usual shearing of arcades shown in panel (a) of Figure 6. Such forces in system B are observed to increase in later data. They are rather strong on the northern side of B on March 24, and on the southern side on March 26. However, no large flares are observed near this current system after March 23; only C-class flares were reported.

The behavior of system A is very different, as a consequence of its different current pattern. The forces here have an important component directed *along* the polarity inversion line. On March 23-24 most of the forces are directed northward, reaching a value of about  $1.9 \times 10^{-3} \text{ N m}^{-2}$  (on the 23), while a few pixels have a southward direction. These forces have a significant component acting against the observed South-westerly motions. Despite drastic changes in the structure of the longitudinal field between March 24 and 25 some of these characteristics of the force remain. In current system A there is transfer of mechanical into electromagnetic energy, but this transfer is very different from that in the usual shear pattern shown in panel (a) of Figure 6. In the period March 23-24 the situation in current system A resembles that depicted in panel (b) of Figure 6. Then, on March 25, the forces are mostly transverse to the southernmost part of the inversion line and diverge. While the earlier behavior persists in the northern part of system A, the southern part evolves toward the same behavior as system B.

We find a maximum value for the magnitude of the forces in Figure 7 of about 1/10 of the gravitational force at the layers where our magnetic field is measured (height  $\sim 250 \text{ km}$  corresponding to  $\rho \sim 6 \times 10^{-5} \text{ Kg m}^{-3}$ ). This horizontal force is large compared with inertial forces, but is small compared with gravity. The energy transfer corresponds, therefore, to horizontal pressure gradients that are smaller than the gravitational pressure gradient. Assuming a scale-height  $h \sim 10^5 \text{ m}$  for the forces (similar to the density scale-height), we find from the observed component of the Lorentz forces in system A that the total horizontal push on the plasma is about  $2 \times 10^{16} \text{ N}$ .

The power "pumped" into magnetic free-energy of the plasma contained in a layer of depth  $h$  at current system A depends on the velocity component parallel to the Lorentz force (but in the opposite direction). Assuming an upper bound for this velocity of  $10^3 \text{ m/s}$ , this power is about  $2 \times 10^{19} \text{ W}$ , i.e.,  $1.7 \times 10^{24} \text{ J/day}$ . The energy buildup over a day is marginally enough to supply the combined energy released in both flares (viz.,  $\sim 10^{31} \text{ erg}$ ). Furthermore, purely horizontal plasma motions of such magnitude would result in

displacements of about  $8.7 \times 10^9$  m/day. The observed umbra's motions are far less, about  $7 \times 10^6$  m/day (corresponding to 80 m/s). It is still possible that larger plasma motions occur outside the umbrae, but it is unlikely that they could exceed  $10^3$  m/s. Thus the observed magnetic free-energy buildup (based on Lorentz forces due to the observed vertical electric currents) is insufficient to power the observed flares. The displacements along the Lorentz forces in current system B are much smaller and therefore the observed energy buildup is much smaller than that in system A.

The rate of observed energy buildup was largest around March 23 at 18:03 UT, decreased somewhat by March 24 at 16:41 UT (but remained high), and become very small on March 26 at 13:59 UT. This buildup appeared related to the source that powered the first flare on March 25 at 08:10; there is no comparable buildup for the second flare on March 26 at 20:35. Thus, the observed buildup that precedes flaring in the current system A cannot be used to forecast later activity. The second flare may result from energy stored in the layers at and/or above the photosphere until it was released one or two days later. The energy for the first flare can also be inferred from the observed large vertical electric currents, but the currents decayed so much by the time of the second flare that they cannot be considered consistent indicators of flare probability.

It is surprising that the high energy buildup in the active region, although insufficient for a major flare, occurs precisely at the location where the flares erupt, and occurs just before the first flare. The observed buildup may be just the residual of a much more important energy storage occurring at deeper layers, or through horizontal currents that cannot be observed with present instrumentation.

The observations indicate that material emerges from deeper layers to the West of the spot N1; it flows around the South side of spot N1 and shears the field. Then the displacements stop; consequently the material must disappear by submerging somewhere to the South-West of spot N1. The previous figure for energy buildup corresponds to stresses on the horizontal component (or more accurately the transverse component) of

the field that produce a shearing of the same type as the observed transverse magnetic field pattern near the polarity inversion line. However, the emergence and submergence of material, if forced by pressure and gravity, respectively, distort the field in a way that corresponds to a buildup of horizontal currents. The work done in such distortions may be substantially larger than the one that we have determined above.

## 7. Discussion

The magnetic field structures of whole flaring active-regions often display large imbalance of the longitudinal field. In the present case this structure can be broadly described by an inclined dipole (Figure 3), and does not change much in the four days we study. The significant changes that can be flare related occur in included polarities with a spatial scale of about an arc min. or smaller. Large localized electric currents are observed near the included polarities. The observed total electric current is unbalanced in the earlier observations.

In the first part of this section we discuss which characteristics of these changes can be used to forecast flares. In the second part we discuss some scenarios for the magnetic free-energy buildup that may account for flares. Finally, we study the amount of energy buildup indicated by the observations, and its implications for the buildup scenarios.

### 7.1. Flare forecasts

The similarity between the X-ray light curve for the first (March 25 at 08:10 UT) and second large flare (March 26 at 20:35 UT) suggests very similar energy releases for the two flares. However, the magnetic configuration, magnetic shear, and electric currents

are conspicuously different in both cases. This can only be explained by assuming that the observed photospheric vertical currents are not those directly responsible for the flaring.

Our data show that flare prediction based only on "magnetic shear" does not predict the time and location of large flares. The first of two large flares occurred not at the highest shear location but at a secondary location of decaying shear. The second flare, of similar yield, occurs in the same region at a time of even lower shear. These considerations are also valid for the magnitude of the vertical electric currents. The largest currents were at locations without significant flaring, and the current was low when the second flare occurred.

We find a remarkable change in the longitudinal field and the current pattern near the time and location of the first X-class flare. At this time, the longitudinal field changes its topology and a null of the potential field appears. The changes are related to motions of secondary sunspots. Also at this time, the electric current changes by: decreasing and shifting away from the polarity inversion line, and becoming more balanced (see Table 3). Changes in the field and vertical currents are absent in the second flare, but instead sudden sunspot motions are observed.

We suggest that the existence of large vertical currents, emerging flux and sunspot motions, are all interrelated indicators of energy transfer from subphotospheric layers. However, the present observations are insufficient for assessing the amount of energy being transferred. To gain further insight we need to complement the observations with indicators of the vertical plasma velocity and the horizontal electric current.

The existence of energy transfer does not determine that a large flare will occur, because the energy can just be dissipated or disperse. We suggest that another condition is required for the magnetic-energy storage, at least for some types of flares: unbalanced vertical currents must exist near the polarity inversion line.

Our observations suggest that a flare is triggered when a magnetic null appears above the photosphere. In our flares, the apparition of the null of the coarse potential field

is accompanied by sudden a change in the vertical currents that implies related changes in the closing currents above the photosphere. These changes only indicate the onset of flaring activity, and the full release of the stored energy may occur throughout several flare events.

The existence of a magnetic null near the flaring location is very important. As shown by Fontenla (1993), in regions near a null the plasma-beta is near or above unity so that large electric currents can be easily raised, such as the ones observed. These motions close to the null would lead to localized sheets of very large current density in which rapid dissipation may occur.

## 7.2. Other energy buildup scenarios

Leka et al (1993), and de La Beaujardiere et al (1993) considered flaring in a magnetic configuration similar to that of the flare models related to prominence eruption (e.g., Kuin and Martens 1990). This is clearly not the case in our flares because: 1) the coarse structure of the field is quite different from a sheared arcade; 2) the vertical electric current is unbalanced and close to the polarity inversion line instead of a pair of opposite currents on both sides of this line; 3) there is no filament signature in the  $H\alpha$  and Ca II data we examined. The part of the active region with the strongest similarity to a sheared arcade was current system B (see Figure 5) which had no large flares. The most conspicuous surging in  $H\alpha$  (see Ambastha, Hagyard and West 1993) was current system C, had no large flares.

Kurokawa (1987) reported  $H\alpha$  observations of sheared fields in two active regions: one with very large flares, similar to our system A; and another without large flares, similar to our system B. Kurokawa suggests that there are two types of sheared active regions, one associated with the "emergence of twisted magnetic flux ropes", and another resulting from the "collision between two sunspots of opposite polarities", as in our systems A and B, respectively. The emergence of material and the sheared field

pattern in our region resemble those shown by Kurokawa. However, we do not describe the situation in this way because from the observations we can only ascertain that the field is sheared but not that there are internally twisted flux ropes.

In our flares, at current system B, the magnetic configuration has a structure in which the field is distorted sideways as proposed by Fontenla and Davis (1991) for flare production. The observed horizontal motions, magnetic shear, and electric currents, and the derived Lorentz forces all coincide with the scenario of Fontenla and Davis (see sketch in Figure 6). The flow pattern, on March 25-26, depicted in Figure 8 (see also *f3*) results from the emergence of plasma and negative field east of the spot N1, and from the migration of the previous positive field toward the South-West. These motions are accompanied by shearing of the transverse magnetic field, and by changes in the longitudinal field.

### 7.3. The rate of energy buildup

The observations reveal important Lorentz forces at the layers where the magnetic field is measured. The horizontal component of these forces can only be fully deduced from the observations close to the polarity inversion line. We find that this component is opposed to the observed horizontal motions. Therefore, these Lorentz forces are a reaction to pressure-driven horizontal plasma motions (note the smallness of inertial effects), and correspond to magnetic free-energy storage. Rough estimates based on the observed parameters give insufficient energy storage to account for the energy released in the flares.

However, the rate of energy buildup was high only at the location of the flare activity and just preceded the start of this activity. Thus, the weak observed energy buildup may be an indication of a stronger energy buildup. It is hard to explain how both flares could arise from the same magnetic process, unless the observed vertical current's

magnitude and distribution are not critical factors. This conclusion contrasts with most flare scenarios in which the vertical current plays a central role.

Horizontal currents are required by MHD theory because of the solenoidal condition of the electric current. Horizontal currents cannot be derived from available observations of photospheric fields, but their structure is critical for magnetic free-energy storage.

A probable solution for the puzzle of the free-energy storage is that it occurs mostly in the form of horizontal currents. Important energy buildup may be associated with the horizontal electric currents due to flow of material. Lorentz forces due to these currents have vertical and horizontal components that we cannot observe, but they can do the work needed. The formation of horizontal currents is naturally expected when plasma and field emerge. Also, "emergence" will force "horizontal flows" and plasma will "subside" elsewhere. Thus, it is not possible to consider independently any of these three components of the overall flow pattern.

The existence of vertical currents at the photosphere implies that horizontal currents must exist above the layers measured. Flares may be produced by a rearrangement of these currents, without change in the vertical currents at the photosphere. This process may release part of the self- and mutual-energy of the currents. These components can be interpreted in a circuit analogy, but in more realistic MHD they have to be more rigorously defined. Fontenla (1993) provides in his Appendix B such rigorous definitions valid in any full MHD case. In this paper Fontenla also develops the theory of current sheet buildup in a magnetic null configuration. Our observations indicate a null in the flaring region. Therefore the observed photospheric motions are expected to produce current sheets. The collapse of such sheets can produce the rapid energy release in the observed flares. However, for modeling of the MHD processes taking place in these flares a two-dimensional approach is not realistic and a three-dimensional approach is



needed. In the three-dimensional case horizontal electric currents can close consistently with vertical currents at a finite distance, and plasma flows can be treated consistently with mass conservation and gravity.

Finally, we also conclude that the observed Lorentz forces pose problems for any attempt to construct force-free extrapolations of the observed field for assessing the magnetic free-energy storage. These difficulties arise because we observe significant non-field-aligned currents that do not fit into any force-free extrapolation. The existence of these currents is logical because the observations correspond to photospheric layers where the plasma-beta is not very small ( $\beta \sim 1$  for the observed field of 800 G at the polarity inversion line where the two flares occurred).

#### Acknowledgments

We acknowledge the Marshall Space Flight Center for providing us with the vector magnetograph data. This work was done while one of the authors, A.A., held a National Research Council-NASA Research Associateship at the Marshall Space Flight Center, Huntsville, AL. One of the authors, J.M.F., acknowledges support from the Solar Physics Branch of the Space Physics Division of NASA, through Grant NAS8-874. We acknowledge advice on the data calibration from the MSFC team, especially M. Hagyard and E. West, and interesting discussions with G.A. Gary. We also acknowledge the referee's advice that helped us improving the presentation.

## Appendix A

### Calculation of the potential field

In the following we will assume a potential field above the photosphere. This hypothesis is known to fail in some regions because vector magnetograms indicate that substantial vertical currents. However, measured vertical currents are often localized, and there are extended regions where the vertical currents are below the measurement noise level. Thus, in many cases the actual structure of the coronal magnetic fields may not differ too much from a potential field.

For computing the magnetic field from the vector magnetic fields measured at the photospheric boundary we developed a scheme that takes into account not only the vertical, but also the horizontal components of the field. The use of the horizontal components partially compensates for the limited field of view and the lack of side and top constraints on the field. In theory, we would be able to define a unique potential function,  $\Phi$ , that accurately describes the magnetic field in a current-free domain, by solving the equations

$$\nabla^2 \Phi = 0 \quad , \quad \bar{\mathbf{n}} \cdot \nabla \Phi = \bar{\mathbf{n}} \cdot \mathbf{B}_S$$

where  $\mathbf{B}_S$  indicates the measured value of the field over the surface  $S$  that fully encloses the simply connected domain.

In practice, however, the magnetograph field of view represents only a limited portion of the enclosing surface. The observed rectangular portion of the photosphere may be considered as the lower boundary of a parallelepiped, in which the normal component of the field is unknown at the sides and top. The potential field results from solving the equations

$$\nabla^2 \Phi = 0 \quad , \quad \bar{\mathbf{e}}_z \cdot \nabla \Phi_p = \bar{\mathbf{e}}_z \cdot \mathbf{B}_p(x, y, z = 0)$$

where  $\mathbf{B}_p$  is the vector magnetic field measured at the photospheric level, i.e., the lower boundary. These equations do not fully determine the potential field. The additional

constraints at the sides and top of the domain are necessary to discriminate among the set of potential fields that satisfy the previous equations.

There have been several methods developed for computing the potential field from observations. Altschuler et al. (1977) assume that the normal component of the field is known at a closed spherical surface at the photosphere; a condition that the field is radial is imposed at an outer, "source", concentric spherical surface. This method resorts to a strong assumption regarding the radius of the "source" surface, and the fact that the field is purely radial there. Furthermore, measurements of the vertical field across the entire solar surface cannot be made at present, and this field is only inferred from synoptic observations over a full solar rotation. This method is well suited for studying the slowly varying global solar magnetic field configuration, but can hardly be justified for studying single dynamic active regions. Other methods for deriving the potential field resort to Fourier expansions; they assume periodic conditions at the sides of the domain. These conditions can hardly be justified because active regions do not repeat themselves. Usually the Fourier expansion methods assume that the field decreases exponentially at the upper boundary. This is also a very strong constraint that is not satisfied by a simple dipolar field, the simplest field representing many observed situations.

The method that we propose consists in using the observed transverse components in selecting between all the possible potential fields that satisfy the previous equations. For this we construct the potential field from a distribution of arbitrarily oriented dipoles that are located at a constant depth below the plane of the observations. This depth,  $H$ , is chosen to be sufficiently larger than the separation between observed pixels, in order to minimize the non-smoothness that arises due to the discrete representation of the sources of the field. The magnetic field in the domain is given by

$$\mathbf{B}(x, y, z) = \sum_i \frac{3\mathbf{r}_i(\mathbf{D}_i \cdot \mathbf{r}_i) - \mathbf{D}_i r_i^2}{r_i^5}$$

where

$$\mathbf{r}_i = (x - x_i, y - y_i, z - H)$$

and where the index  $i$  denotes each of the dipoles that are assumed to be the sources of the field. In our present calculations these dipoles are located beneath of the center of each of the pixels (or rather of the group of observed pixels since we have performed some averaging). For our current calculations we have set  $H$  to be twice the separation between pixels, i.e.,  $H \approx 22$  arc sec, and we find that this provides sufficiently smooth solutions to prevent sharp changes of the field in between the centers of the pixels. The three components of the dipole strengths are determined from the data, but the horizontal components are substantially noisier than the vertical. Moreover the observations of the horizontal field have an inherent ambiguity of  $180^\circ$ .

Therefore, we performed an iterative procedure in which we initially assume that the dipoles have only vertical components. By inverting a linear system of equations we derive the magnitude of the dipoles such that the potential field would match the observed. This corresponds to solving

$$Bz_j = \sum_i Dz_i^0 \frac{3H^2 - r_{i,j}^2}{r_{i,j}^5}$$

Then, the vertical component of the source dipoles that was previously determined is used to compute the horizontal components of the potential field corresponding to the previous iteration. This horizontal potential field is compared with the observed. At each iteration the  $180^\circ$  ambiguity in the direction of the measured field is resolved by minimizing the angle between the observed and computed fields. The errors of the computed horizontal field are corrected by introducing horizontal components of the source dipoles. These components are determined such that they, together with the previously determined

vertical components, produce a horizontal field that matches the observed. This corresponds to solve the following linear system of equations

$$Bx_j - \sum_i Dz_i^{n-1} \frac{3x_{i,j}H}{r_{i,j}^5} = \sum_i Dx_i^n \frac{3x_{i,j}^2 - r_{i,j}^2}{r_{i,j}^5} + \sum_i Dy_i^n \frac{3x_{i,j}y_{i,j}}{r_{i,j}^5}$$

$$By_j - \sum_i Dz_i^{n-1} \frac{3y_{i,j}H}{r_{i,j}^5} = \sum_i Dy_i^n \frac{3y_{i,j}^2 - r_{i,j}^2}{r_{i,j}^5} + \sum_i Dx_i^n \frac{3y_{i,j}x_{i,j}}{r_{i,j}^5}$$

Since the now determined horizontal components of the dipoles also affect the vertical field, the current iteration vertical components of the dipoles is found by solving the following equations

$$Bz_j - \sum_i Dx_i \frac{3Hx_{i,j}}{r_{i,j}^5} - \sum_i Dy_i \frac{3Hy_{i,j}}{r_{i,j}^5} = \sum_i Dz_i^n \frac{3H^2 - r_{i,j}^2}{r_{i,j}^5}$$

The resulting three components of the source dipoles provide a potential field which accurately matches the observed vertical field, but whose horizontal field does not accurately match the horizontal fields.

After a few iterations in this procedure the mismatch in the horizontal fields decreases substantially, then remain unchanged. Most of our computations use a field of view of  $\sim 232 \times 174$  arc sec, represented by  $20 \times 15$  pixels (corresponding to  $80 \times 60$  pixels in the unsmoothed data). These computations were carried in a VAX computer and require considerable memory. Calculations were also carried using half of the previous smoothing, and with  $40 \times 30$  pixels. The higher resolution calculations show more detail but no significant differences for the selected active region.

Our procedure was carefully tested by setting up artificial data derived for the field from a simple dipole source buried somewhere under the observation's plane. When the dipole source is located too far down compared with the size of the field of view, large errors in the estimate of the potential field occur at some height above the plane of

observations. When the source of the field is brought near the plane where we set up the dipoles for approximating the potential field, the artificial distribution of dipoles reduce to having only one dipole with the magnitude and orientation corresponding to the source of the actual field. In this case the approximation to the potential field converged to the real potential field with high accuracy. In all cases, when modeling a potential field with null error artificial data we obtained convergence to a reasonably approximate solution. We have modeled some artificial data in which electric currents were built in. The iterative procedure initially converges, but then it reaches a point where it ceases to converge. The residual rms departures of the estimated from the measured horizontal field depend on the currents; this residual is a measure of non-potential behavior. In all calculations using artificial data we found that our method gave an overall structure of the field that behaved more like the real field than calculations using other methods, such as Fourier expansion, monopole distributions, or purely vertical dipole distributions.

We conclude from these test calculations that an approximate potential can be set up by using the transverse components of the measured field. This procedure selects among the potential fields that match the measured longitudinal fields over the magnetograph field of view. The selection is not arbitrary but is based on the observed transverse fields. The potential field from our method can be obtained in all cases, has an overall structure that is reasonable and, unlike other methods, is not much affected by the flux imbalance in the field of view.

## Appendix B

## The evaluation of electric currents

We derive the electric current density from magnetograms by using Ampere's law in its integral form,  $\mu_0 I_z = \int \mathbf{B} \cdot d\mathbf{l}$ . The integration we use interpolates the vector transverse fields between each group of four adjacent pixels, and assumes that the current is uniformly distributed within the enclosed area. This gives the vertical current density values  $J_z = I_z/S$ , where  $S$  is the area of the enclosed surface, and the current density value is assigned to the center of the area. This determination gives only a lower bound on the current density, because a much larger current density may be highly localized within the pixel separation and produce the same result. However, the net unbalanced current within the resolution area is accurately derived from our estimates (except for errors in the transverse field measurement).

The determination of the electric current must resort to some scheme to resolve the  $180^\circ$  ambiguity of the direction of the transverse field. Our scheme assigns the direction of the observed transverse field in such a way that the angle between observed and potential fields is less than  $90^\circ$ . This criterion is somewhat arbitrary and implies an assumption on the upper bound of the magnitude of the electric current. Moreover, in highly sheared regions the application of this criterion produces a definite answer even in the case of an ambiguity between angles of  $89^\circ$  or  $-91^\circ$ . In this last case, it is hard to make any local argument for selecting the lower absolute value of the angle. Another scheme to resolve the ambiguity, used by Gary and Demoulin (1993) for similar data, resulted in basically the same electric current pattern (see their Figure 2). This and the fact that similar patterns are observed when comparing different data sets gives us confidence in the significance of the patterns depicted by our Figure 5.

Assuming an uncertainty in the transverse field of  $\Delta B \approx 100$  G, the maximum noise level in our data can be estimated to be about  $(2\Delta B)/(a\mu_0) \approx 10$  mA/m<sup>2</sup>. However, observations show that the actual noise level is  $\sim 4$  mA/m<sup>2</sup>.



Table 1

The sunspots maximum field on March 23

Spot	Longitudinal field in Gauss	Denomination in Ambastha et al 1993 (Figure 2)
P1	1126	P1
N1	-2155	F1
N2	-1965	F2
N4	-1266	F4
P2	518	P2
N3	-1298	-
P3	1455	P3
N5	-1537	F5
P4	813	P4
N6	-1454	F7
P5	1832	P5

Table 2

The nulls in the region above IP1

Date	Time	Height	B <sub>min</sub>
1991 March 23	18:03 UT	-	-
1991 March 24	16:41 UT	2,500	7 G
1991 March 25	13:57 UT	2,000	0
1991 March 26	13:59 UT	1,800	0

Table 3

The main electric currents on March 23, 1980

	Total upflowing current (A)	Total downflowing current (A)	Maximum upflowing current density (mA m <sup>-2</sup> )	Maximum downflowing current density (mA m <sup>-2</sup> )
System A	$1.2 \times 10^{13}$	$3.3 \times 10^{12}$	40	33
System B	$2.1 \times 10^{12}$	$1.7 \times 10^{12}$	22	33
System C	$2.4 \times 10^{12}$	$2.5 \times 10^{12}$	17	21

## References

- Altschuler, M.D., Levine, R.H., Stix, M., & Harvey, J.W. 1977, *Solar phys.*, 51, 345.
- Ambastha, A., Hagyard, M.J., & West, E.A. 1993, *Solar Phys.*, in press.
- de La Beaujardiere, J.-F., Canfield, R.C., & Leka, K.D. 1993, *ApJ*, 411, 378.
- Demoulin, P., Henoux, J.C., & Mandrini, C.H. 1992, *Solar Phys.*, 139, 105.
- Fontenla, J.M., & Davis J.M. 1991, *Bull. Am. Astron. Soc.*, 23, 1067.
- Fontenla, J.M. 1993, *ApJ*, in press.
- Gaizauskas, V. 1989, *Solar Phys.*, 121, 135.
- Gary, A.G., & Demoulin, P. 1993, in *Proceedings of the XIV NSO/SP Int. Summer Workshop, PASP*, in press.
- Hagyard, M.J., Smith, J.B., Teuber, D., & West, E.A. 1984, *Solar Phys.*, 91, 115.
- Heyvaerts, J., Priest, E., & Rust, D.M. 1977, *Solar Phys.*, 53, 255.
- Kalman, B. 1980, Thesis, Pulkovo.
- Krall, N.A., & Trivelpiece, A.W. 1973, *Principles of Plasma Physics* (New York:McGraw-Hill).
- Kuin, P., & Martens P. 1990, *ApJ*,
- Kunzel, H. 1960, *Astron. Nachr.*, 285, 271.
- Kurokawa, H 1987, *Solar Phys.*, 113, 259.
- Leka, K.D., Canfield, R.C., McClymont, A.N., de La Beaujardiere, J.-F., Fan, Y., & Tang, F. 1993, *ApJ*, 411, 370.
- Livi, S.H.B., Martin, S., Wang, H., & Ai, G. 1989, *Solar Phys.*, 121, 197.
- Machado, M.E. 1987, *Solar Phys.*, 113, 57.
- Newton, H.W., & Num, M.L. 1951, *Month. Not. R.A.S.*, 111, 413.
- Spicer, D.S. 1981, *Solar Phys.*, 70, 149.
- Sturrock, P. 1980, *Solar flares*, Colorado Assoc.Univ. Press.
- Svestka, Z. 1976, *Solar flares.*, Reidel.

Tandberg-Hanssen, E., & Emslie, A.G. 1988, *The physics of solar flares*, Cambridge Univ. Press.

Teuber, D., Tandberg-Hanssen, E., & Hagyard, M.J. 1977, *Solar Phys.*, 53, 97.

Sakurai, T. 1989, *Solar Phys.*, 121, 347.

Zirin H., & Liggett, M.A. 1987, *Solar Phys.*, 113, 268.

### Figure captions

Figure 1. White light images on 1991 March 23 at 18:03 (left panel), and March 26 at 13:59 (right panel). The main sunspots are labeled, and their coarse evolution is evident comparing the two panels. Celestial North is upwards, and the field of view is about  $7 \times 7$  arc min.

Figure 2. The longitudinal magnetic fields for the period March 23-26, 1993. The panels correspond, from left to right and top to bottom, to March 23 at 18:03 UT, March 24 at 16:41 UT, March 25 at 13:57 UT, and March 26 at 13:59 UT. For the upper series of frames the gray-scale is such that the whitest shade corresponds to the maximum positive field and the darkest shade corresponds to the largest absolute value negative field. For the lower series of panels we have chosen saturation levels of  $\pm 200$  G in order to display the weaker fields. Again celestial North is upwards, and the field of view is about  $6 \times 6$  arc min.

Figure 3. Scheme showing a way in which the overall large scale field can be represented by a tilted submerged dipole. The vertical negative flux is very concentrated and leads to a large field in a relatively small region, while the positive flux is very spread and corresponds to weak fields. Note that the field to the East is mostly horizontal.

Figure 4. Scheme showing the sunspot motions for the period between 1991 March 21-26. The arrowheads show the positions of the umbrae at 12:00 UT on each day, and the directions of the arrows indicate the direction of motion. The motions are shown relative to the position of the largest field umbra, N1, that is indicated with a cross. Panel (a) shows the umbrae's positions, and panel B shows the intensity contour shapes on March 23, reduced to the heliographic Carrington System. Many of the small umbrae whose displacement is shown here were not labeled before, and one of these umbrae to the South of N1 has positive field and displaces crossing the path of the spot P1.

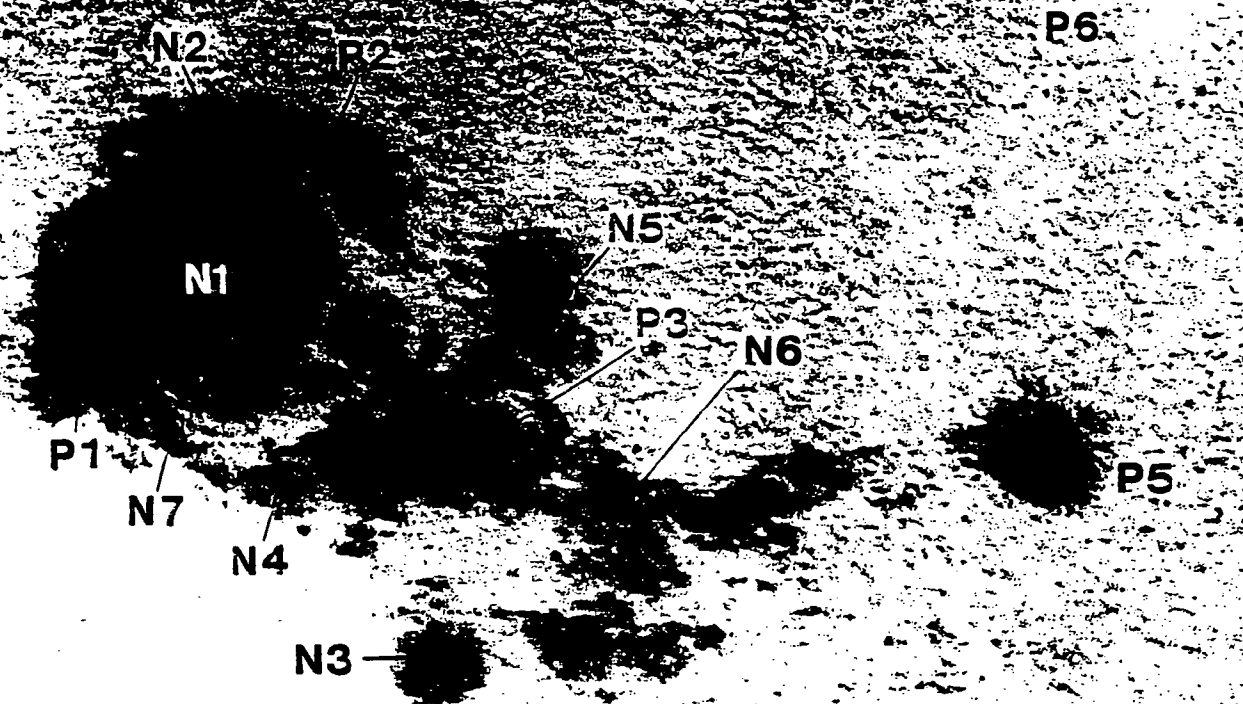
Figure 5. The contour levels for the electric current density corresponding to the observations shown in Figure 2. The solid lines correspond to upflowing currents and the short-dash lines correspond to downflowing currents. The long-dash lines correspond to the polarity inversion lines. This map was obtained by smoothing the original data by averaging over  $2 \times 2$  pixel ( $\sim 4,000 \times 4,000$  km<sup>2</sup>) areas. The current contour levels start at 4 mA/m<sup>2</sup>, and are separated by that same amount.

Figure 6. Scheme comparing: (a) the usually adopted shear of simple arcades across a longitudinal field inversion line, (b) the form of shear that was proposed by Fontenla and Davis (1991). This figure shows a view down towards the photosphere and illustrates the distortion that a straight field line would experience under the shown velocity patterns. We also indicate the electric currents that correspond to the distortions of the field.

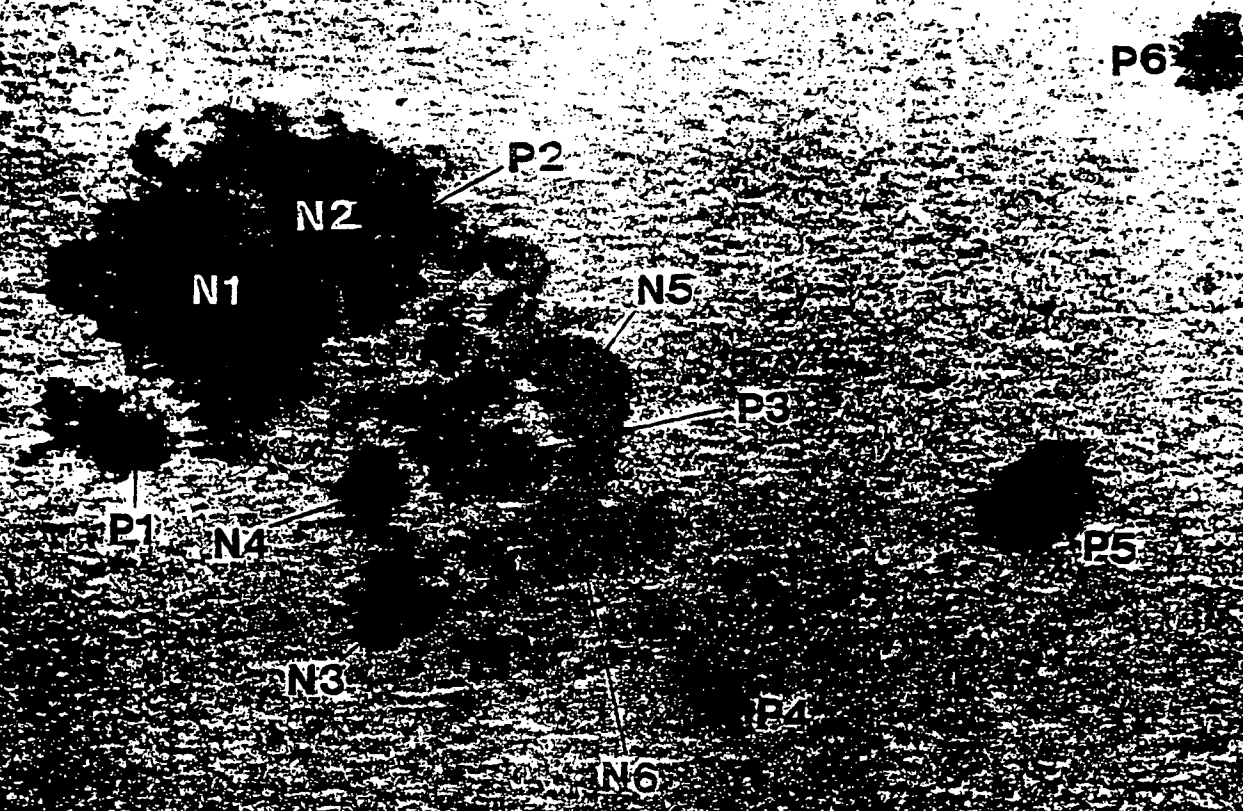
Figure 7. Arrows showing the Lorentz force component that results from the longitudinal (practically vertical) electric currents in Figure 6, and the corresponding transverse (practically horizontal) magnetic field. The contours correspond to the longitudinal field levels of  $\pm 100$  G and  $\pm 1000$  G. The forces computed correspond precisely to the total transverse component of the Lorentz force only at the locations where the longitudinal field vanishes. Wherever a longitudinal field component is present there may be another component to the transverse Lorentz force due to the product of the longitudinal field with the transverse electric current (that is unknown). The longitudinal component of the Lorentz force is unknown, and is due to the product of the transverse components of the field and the current.

Figure 8. Sketch showing the mass flows indicated by the observations. Material emerges to the surface at the location indicated with the dot in a circle, flows horizontally around the spot N1, and submerges at the location near P3 that is indicated with a cross in a circle. The sunspot P1 also moves horizontally but with a smaller displacement. The horizontal velocity is maximum close to the polarity inversion line between N1 and P1, where large shear of the field occurs.

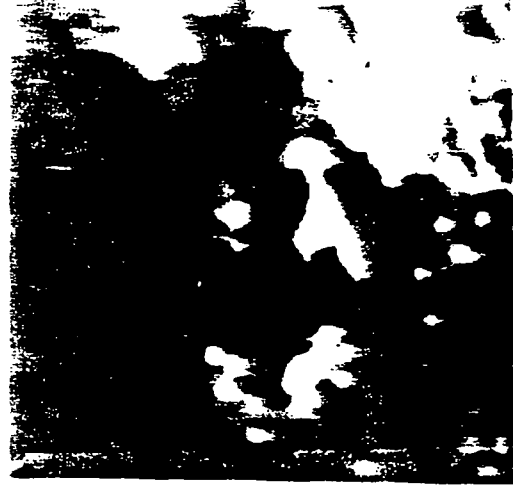
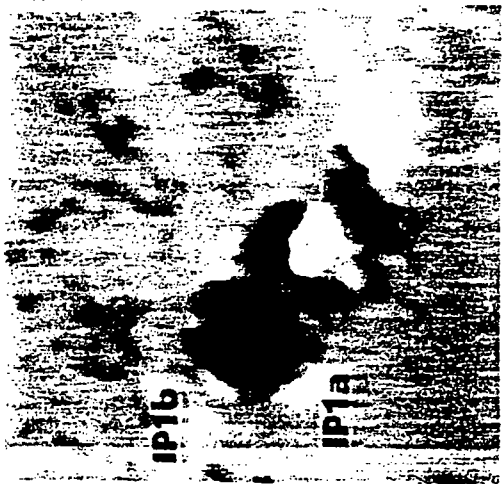
1991 March 23 15:03 UT



26, 14:03 UT







ORIGINAL PAGE IS  
OF POOR QUALITY

6x6

Fig. 2

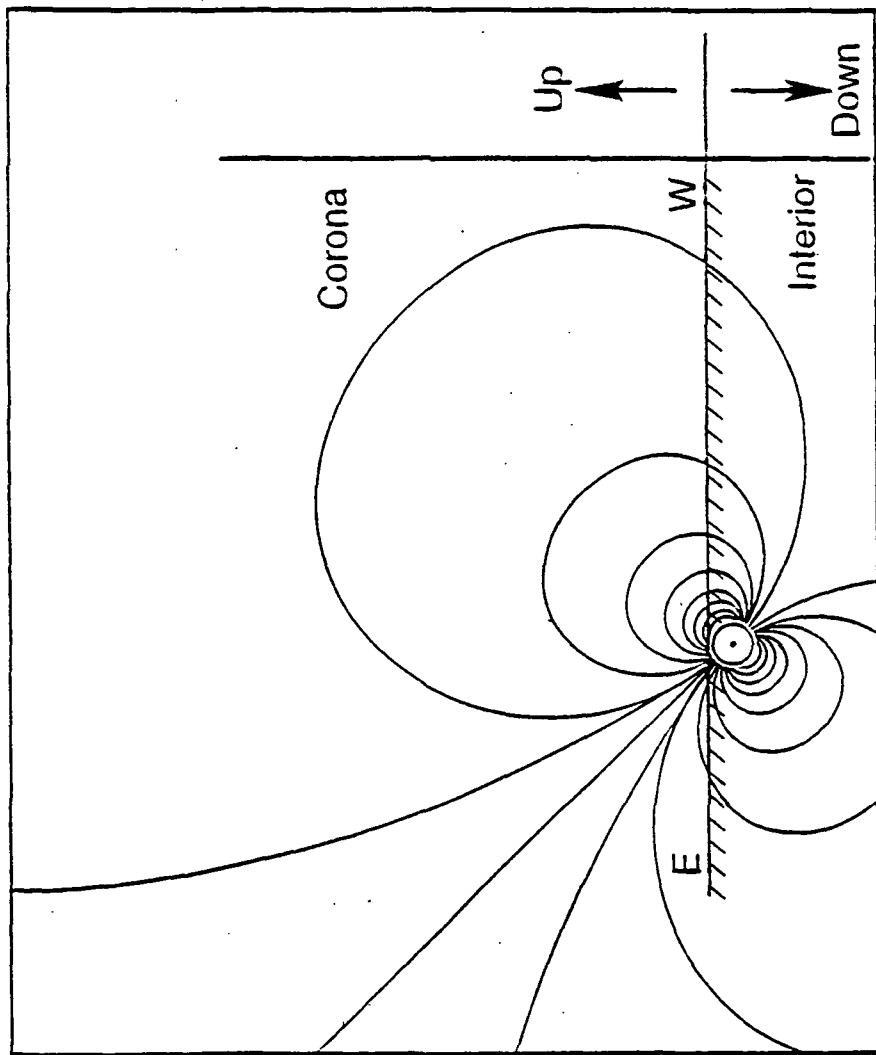
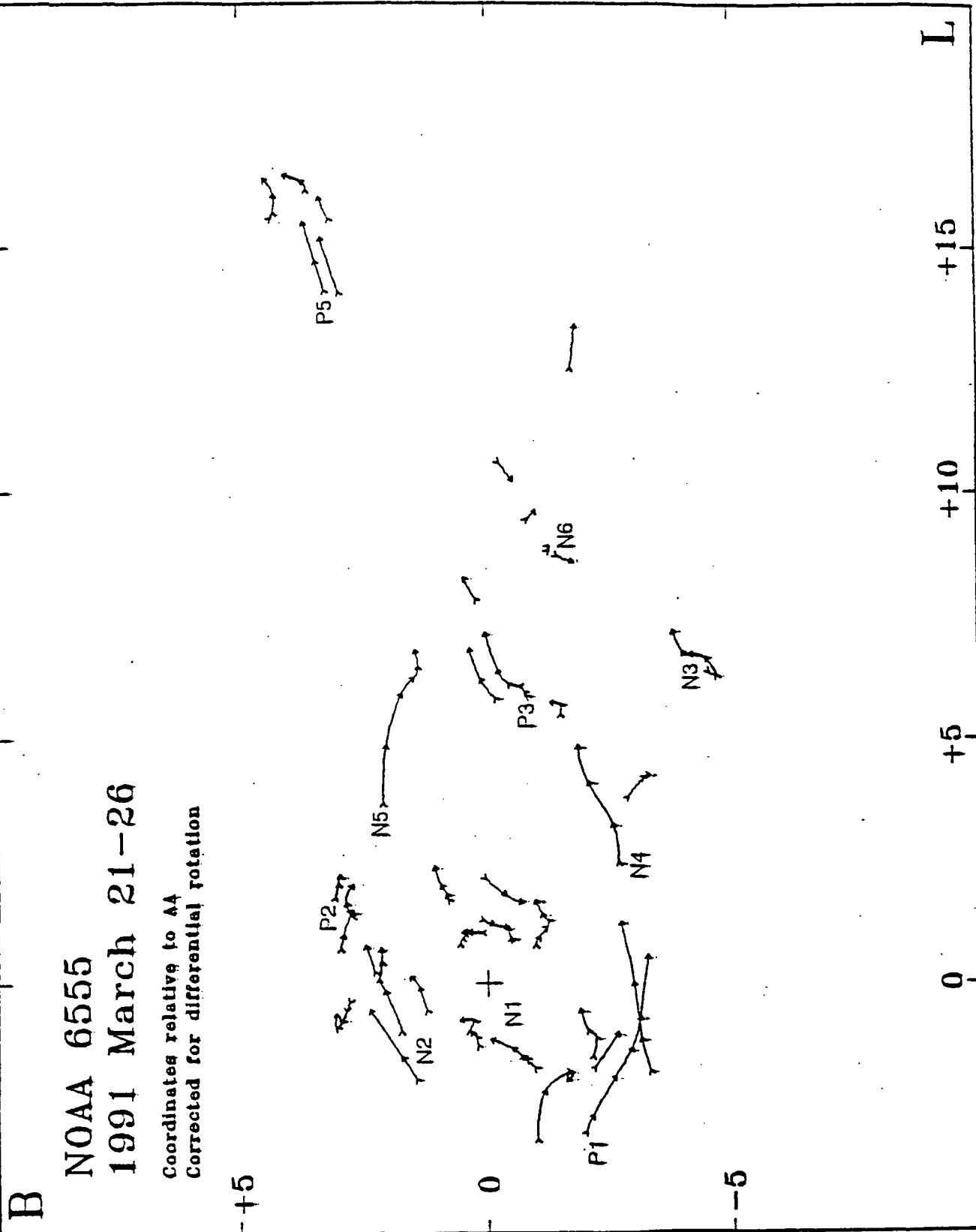


Fig. 3

Fig. 9a



B.

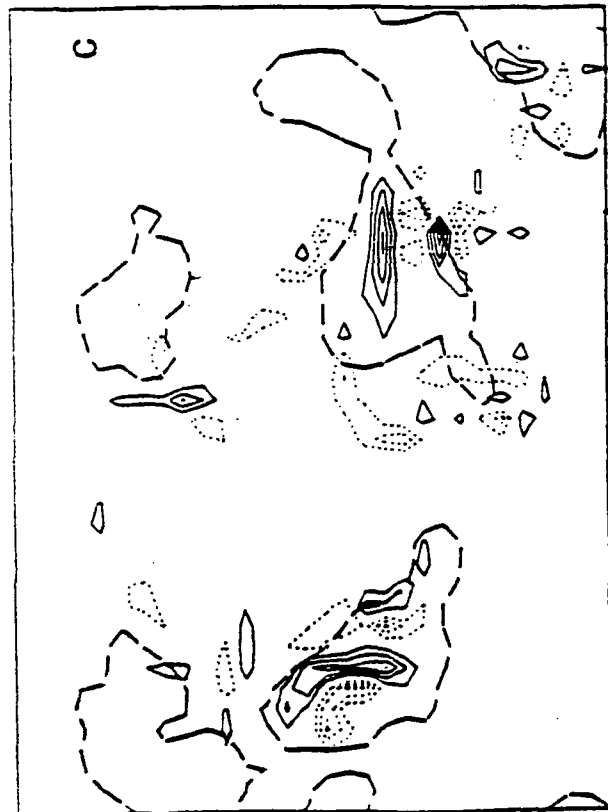
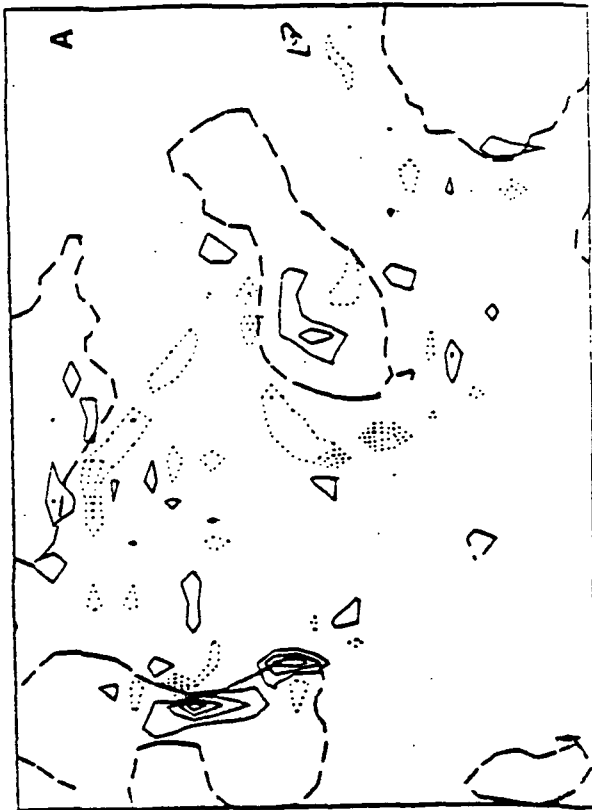
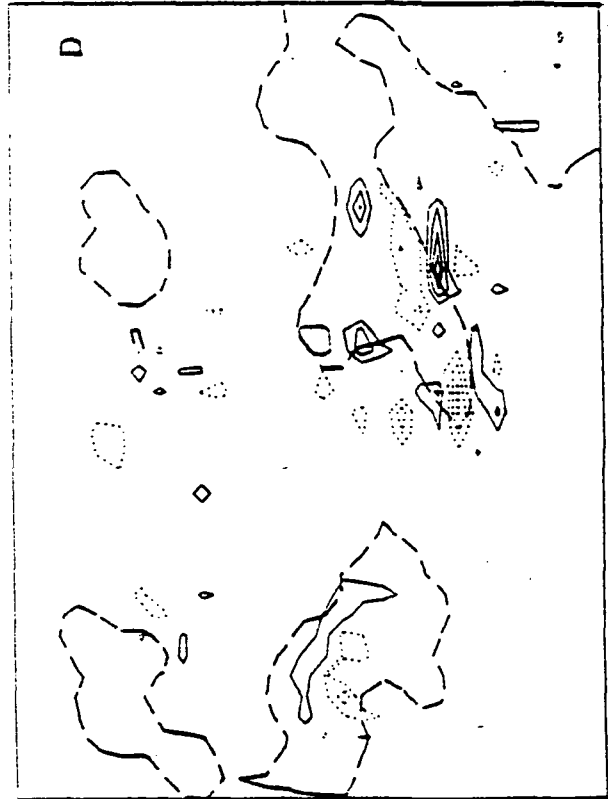
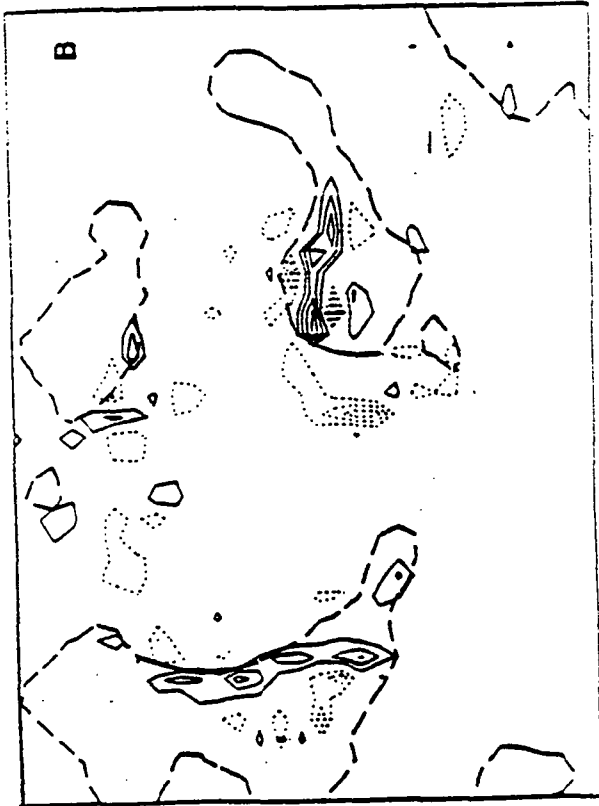
NOAA 6555  
1991 March 23, 15:03:28 UT

Corrected for differential rotation

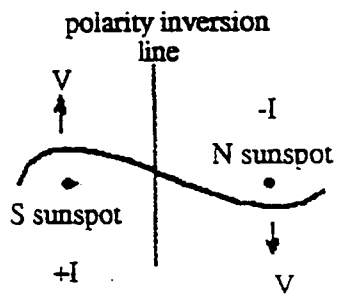


UP A

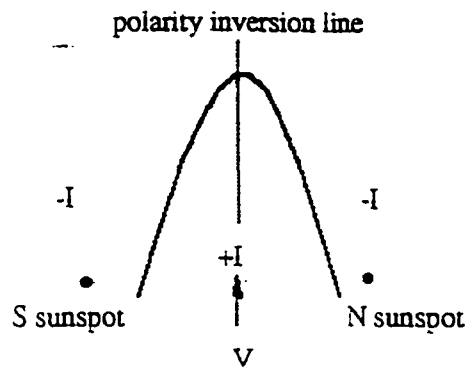
(78) P. 6



PRECEDING PAGE BLANK NOT FILMED



(a)



(b)

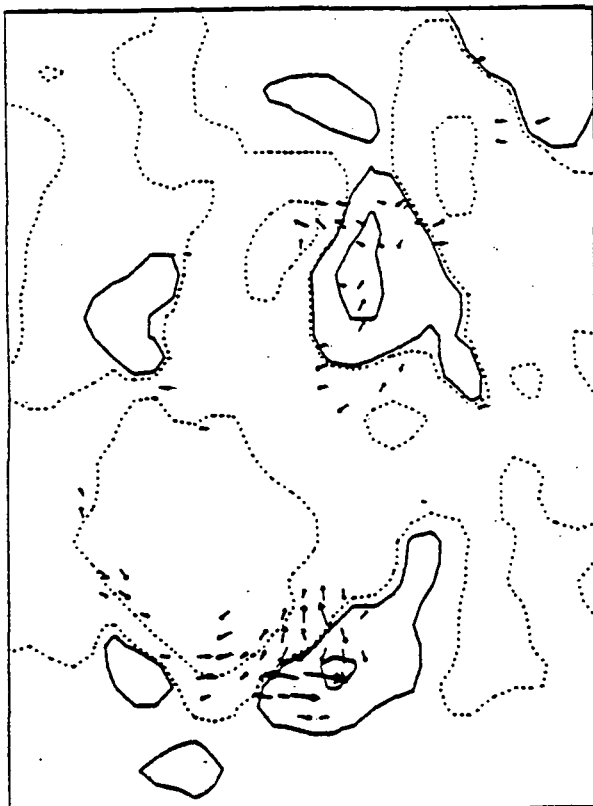
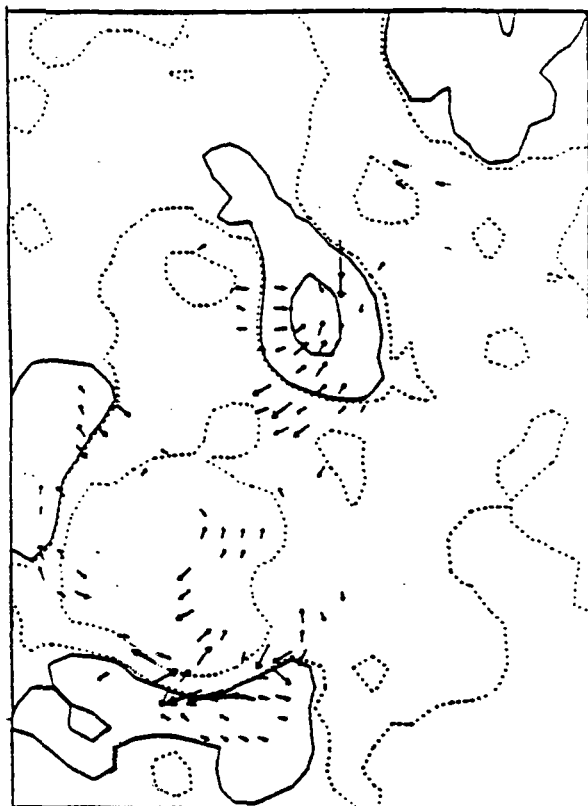
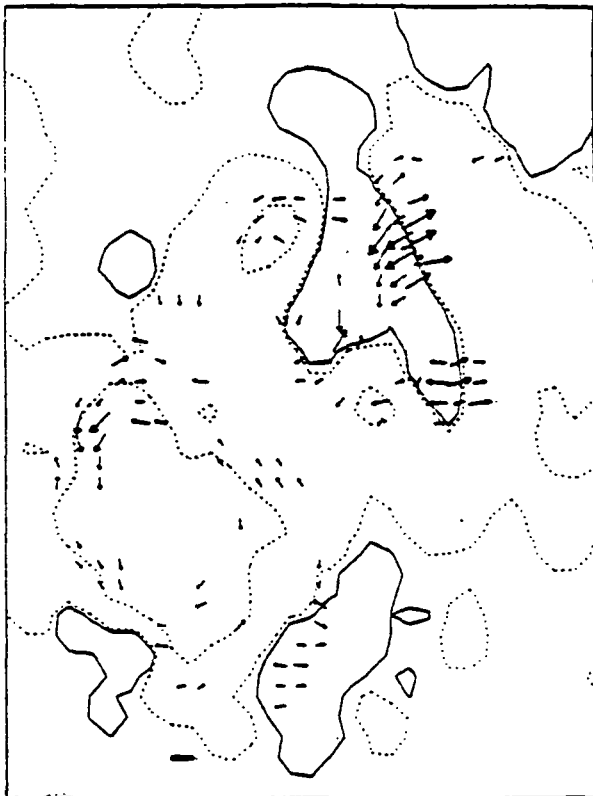
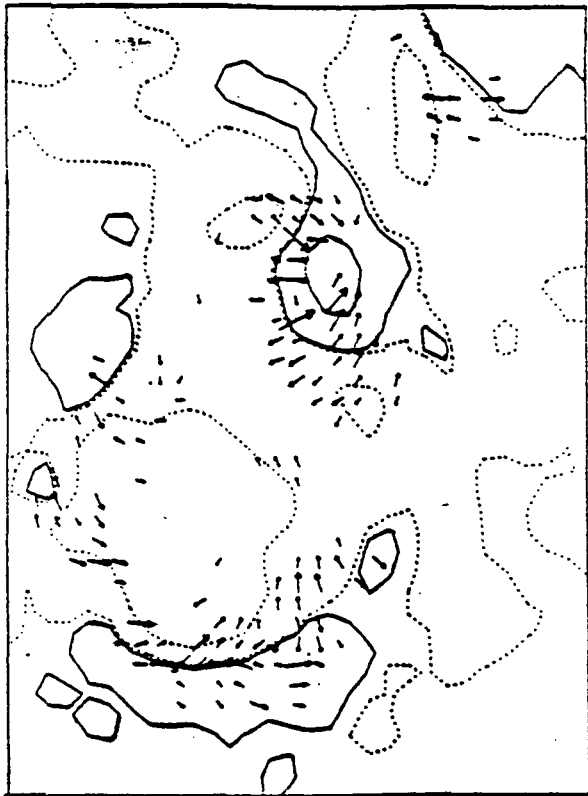
Figure 7

U  
↑

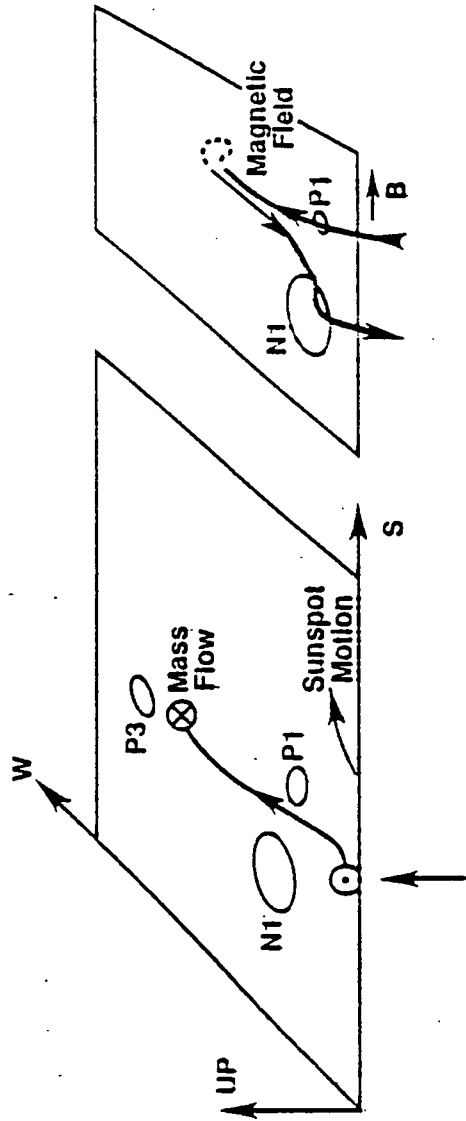
UP

0511

1701



SECRET



UP  
A

Figure 9